


Impact of rare earth (La^{3+}) doping on structural, morphological, optical and dielectric properties of NdVO_4 nanoparticles

M Sharma¹, B Raina¹, M Solanki², B Parekh² and K K Bamzai^{1*} 

¹Crystal Growth & Material Research (CGMR) Lab, Department of Physics, University of Jammu, Jammu 180006, India

²Department of Physics, Pandit Deendayal Energy University, Raisan, Gandhinagar, Gujarat 382426, India

Received: 24 March 2023 / Accepted: 01 November 2023 / Published online: 11 December 2023

Abstract: The present work reports the synthesis of $\text{La}_x\text{Nd}_{1-x}\text{VO}_4$ where $x = 0, 0.05, 0.10$ and 0.15 by a solution based co-precipitation method at $\text{pH} = 12$ calcined at 650°C in nanoparticle form. The novelty of the present work is preparation and various applications of targeted materials by using a traditional liquid-based technique at room temperature without use of any surfactants. The structural, morphological, optical and luminescent properties of as-obtained compositions were characterized by various techniques such as powder X-ray diffraction (PXRD) followed by Rietveld refinement, high-resolution transmission electron microscopy (HRTEM) with selected area electron diffraction (SAED), ultraviolet–visible spectroscopy, Fourier transform infrared spectroscopy and photoluminescence spectroscopy. The PXRD diffraction patterns confirmed tetragonal structure with crystallite size ranging between 22 and 35 nm for all four compositions. The PXRD results are further validated by Rietveld refinement method with low values of profile parameters. HRTEM supplemented with SAED analysis revealed that with a change in doping concentration, there is a change in morphology from rod-shaped to porous hexagonal-shaped features. The optical band gap values are found to be in the range of wide-band semiconductors (2–4 eV). The dielectric properties of as-prepared La-doped NdVO_4 nanoparticles were investigated. The dielectric constant is low in $x = 0.0$ composition, whereas it increases with an increase in La^{3+} concentration.

Keywords: Neodymium vanadate; Rare earth dopant; Co-precipitation; Rietveld analysis; High-resolution transmission electron spectroscopy

1. Introduction

Rare earths are extensively used for a variety of applications leading to their use as rare earth elements (REE) and their alloys in several technological gadgets such as rechargeable batteries, autocatalytic converters, supermagnets, fluorescent materials and many more [1]. Now, if nanoparticles (NP) of these rare earth-based composites are considered, then it shows novel properties compared with other available materials used for various applications. In addition, these NPs show low toxicity and high thermal and chemical stability. Also, when compared with other luminescent NPs, these show fairly high luminescence quantum yield, high photostability and sharp emission bands [2].

Rare earth vanadates as such are a class of multifunctional materials because these exhibit excellent physical

and chemical properties owing to their unique 4f electronic structure. These are suitable for various potential applications such as highly efficient laser diode pumped micro-lasers, low-threshold laser hosts, polarizer materials, efficient phosphors and possessing magnetic and bio-imaging capabilities [3–6]. Particularly, vanadates (VO_4^{3-}) have good potential for acting as host for luminescent applications [7]. Recently, during the COVID pandemic, rare earth orthovanadate was used as electrochemical probe for the precise quantification of various pharmaceutical compounds as these are remarkable for their fundamental and technological significance [8]. Among the rare earth vanadates, neodymium vanadate (NdVO_4) crystallizes in a tetragonal structure and is composed of a slightly distorted tetrahedral VO_4^{3-} ion and rare earth ion Nd^{3+} between the neighboring tetrahedral [9]. It is an important member of the family of rare earth vanadate and is labeled as one of the most promising candidates in the class of functional materials, currently attracting a lot of attention from the

*Corresponding author, E-mail: kkbamz@yahoo.com

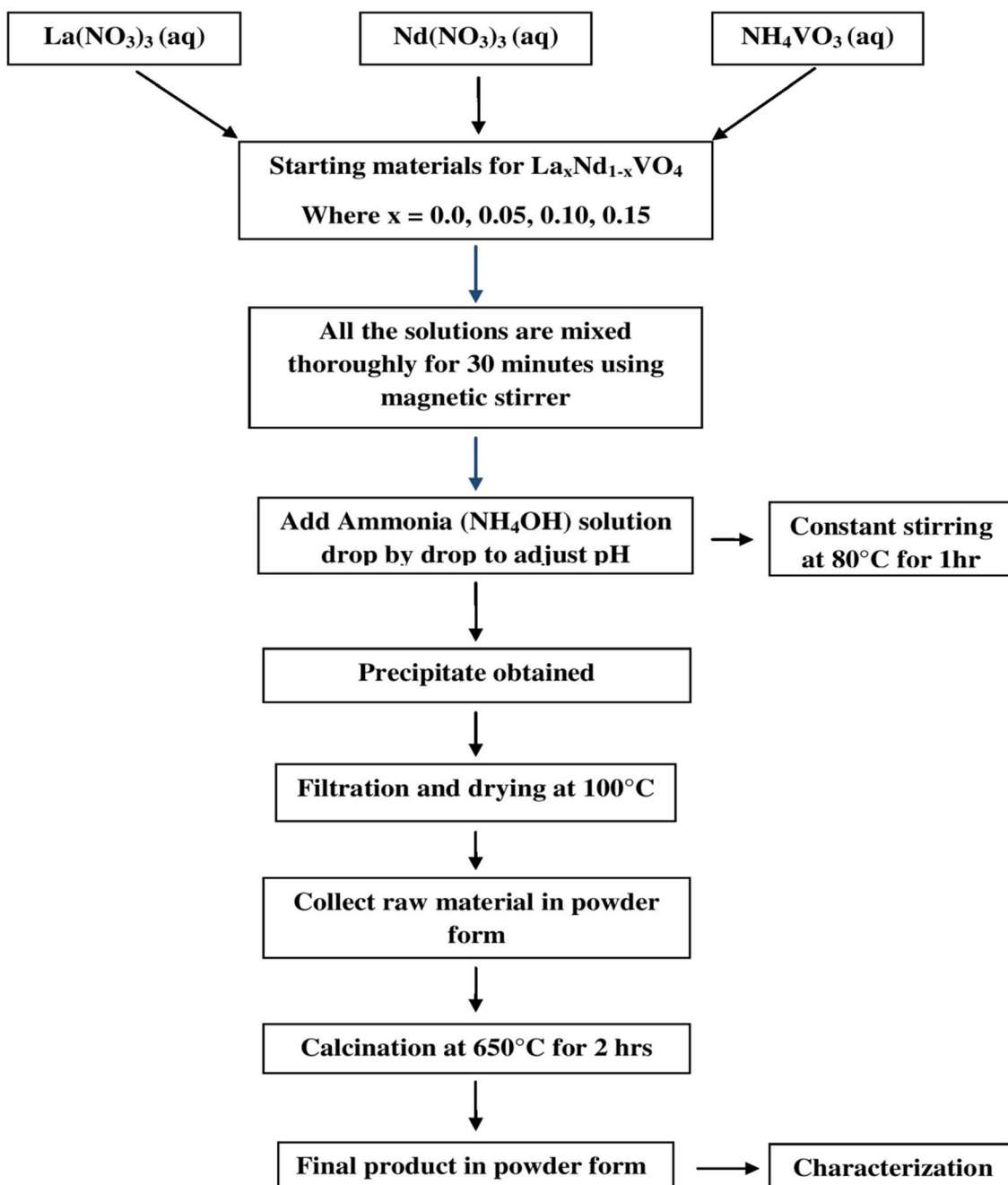


Fig. 1 Schematic view of the synthesis procedure employed to obtain tetragonal $\text{La}_x\text{Nd}_{1-x}\text{VO}_4$ nanoparticles (where $x = 0.0, 0.05, 0.10$ and 0.15)

researchers worldwide due to its unique and distinctive properties and potential applications [10, 11]. Balasubramanian et al. [12] fabricated neodymium vanadate integrated with boron-doped carbon ($\text{NdVO}_4/\text{B-C}$) hybrid composites to utilize as electrochemical sensors for monitoring toxic drug pollutants. Dragomir and Valant [13] prepared a tetragonal NdVO_4 nanoneedle via a simple room temperature precipitation method in the absence of any surfactant. Saad and Ehlag [14] studied the structural,

magnetic, electronic and optical properties of cubic rare earth vanadate perovskites PrVO_3 and NdVO_3 . Tian et al. [15] fabricated tetragonal structural (T-NdVO_4) nanorod arrays doped with Eu^{3+} by a simple one-pot hydrothermal method. Neodymium vanadate nanostructures were successfully synthesized via a modified solid-state method in the presence of ligand by Monsef et al. [16]. Nunez et al. [17] focused their research on Nd-doped LaVO_4 nanoparticles functionalized with poly(acrylic acid) and prepared

from lanthanide and vanadate precursors. Eu³⁺-doped YVO₄ phosphor synthesized by combustion and solid-state reaction was reported by Kumari et al. [18]. Semi-conductive nanometer sized NdVO₄ was synthesized by Kamble et al. [19] using the solution combustion reaction method. Ying et al. [20] reported cerium-doped NdVO₄ nanorods synthesized via a facile one-step hydrothermal method. Thakur and Gathania [21] reported the optical properties of Eu³⁺-doped YVO₄ nanophosphors at different europium concentrations. Vosoughifar et al. [9] reported a novel facile precipitation route for the synthesis of neodymium vanadate nanoparticles with the aid of ammonium metavanadate, neodymium (III) nitrate and lucien as the starting reagents and water as the solvent. Saloni and Khanna [22] reported solid-state sintering to synthesize rare earth-doped YVO₄. Ghotekar et al. [23] reported CeVO₄ nanoparticles with different shapes and sizes fabricated via facile approaches. Aijiang et al. [24] synthesized a novel egg-shaped GdVO₄ for photocatalyst and supercapacitors applications.

So, from these literature surveys, we find some reports on the nanoparticle formation of rare earth vanadates in pure and doped form prepared by different methods. To the best of our knowledge, no studies on the effect of lanthanum (La) on the NdVO₄ nanoparticles have been reported. Lanthanum has been selected as a dopant due to its various excellent properties leading to the enhancement of various properties desired in grown materials. It finds use in the field of optics as lenses and radiation absorbing glasses, particularly in the production of optical glasses like the infrared absorbing glass, camera and telescope glasses. In addition, it is used for the production of catalysts and also in the polishing of glass. Researchers have also reported that the lanthanum-based nanoparticles have the capacity to be used as luminescent materials and as a high dielectric constant lanthanum substituted ceramic material for their possible applications at microwave frequencies [25, 26]. Also, another factor involved in choosing lanthanum as a dopant is their ionic radius which is comparable to that of the neodymium ion.

The present work is focused on the preparation and various applications of pure and La³⁺-doped NdVO₄ (La_xNd_{1-x}VO₄, where $x = 0.0, 0.05, 0.10, 0.15$) nanoparticles without the use of any surfactants at room temperature by co-precipitation technique which makes use of cheap and non-toxic solvent. This method is very convenient and time saving and does not involve any thermal treatment. So, the novelty of the present work lies in the application of a simple and cost-effective solution based room temperature technique to prepare neodymium vanadate and lanthanum-doped neodymium vanadate nanoparticles so that various properties of these materials can be

studied in depth and can be employed for various potential applications.

2. Experimental details

2.1. Synthesis of NdVO₄:La³⁺ nanoparticles

The wet chemical precipitation process was employed for the synthesis of nanoparticles of pure and La³⁺-doped NdVO₄ in an equimolar ratio. The precipitation procedure for the preparation of said materials employed in this study is summarized in the scheme depicted in Fig. 1. La³⁺ ion concentration was set to 0, 5, 10 and 15 mol% with respect to the appropriate Nd³⁺ molar content. Analytical reagents La(NO₃)₃ (99.99%, Sigma-Aldrich), Nd(NO₃)₃ (99.99%, Sigma-Aldrich) and NH₄VO₃ (99.5%, Alfa Aesar) were used as the starting materials. Transparent solutions were obtained by dissolving stoichiometric amounts of La(NO₃)₃ and Nd(NO₃)₃ in distilled water at room temperature. NH₄VO₃ as a source of vanadium ions was dissolved in distilled water at room temperature. Thereafter, these two solutions were continuously stirred at room temperature for 45 min. In the next step, NH₄OH solution was added to adjust the pH to 12 with vigorous stirring at approximately 80 °C on the stirring plate. The white-yellowish precipitate obtained was centrifuged and washed several times with water and ethanol. The obtained as-prepared precipitate was dried for 120 min at 100 °C in air and then calcined at 650 °C for 120 min in the laboratory furnace. In this way, nanoparticles of pure and La³⁺-doped NdVO₄ in powder form were obtained.

2.2. Characterization

Characterization of materials is done to provide information on the structure, elemental composition, optical and other physical and chemical properties of the compositions prepared. The phase structure of the products was studied using powder XRD diffractometer Bruker D8 Advance having a step size of 0.020° and total time/step of 38.40 s and recorded in the 2θ range between 10° and 80°. The refinement of diffraction data was performed through the Rietveld refinement technique using Full-proof software. High-resolution transmission electron microscopy was performed to study the surface morphology using HRTEM: Jeol/JEM 2100 working at 200 kV using a LaB₆ electron gun with a point resolution of 0.23 nm and a lattice resolution of 0.14 nm. Selected area electron diffraction (SAED) pattern was also recorded. The functional groups of the prepared samples were studied by FTIR spectrometer using the Thermo Nicolet iS50 recorded in the range of 4000 cm⁻¹ to 400 cm⁻¹. UV-Vis spectroscopy was

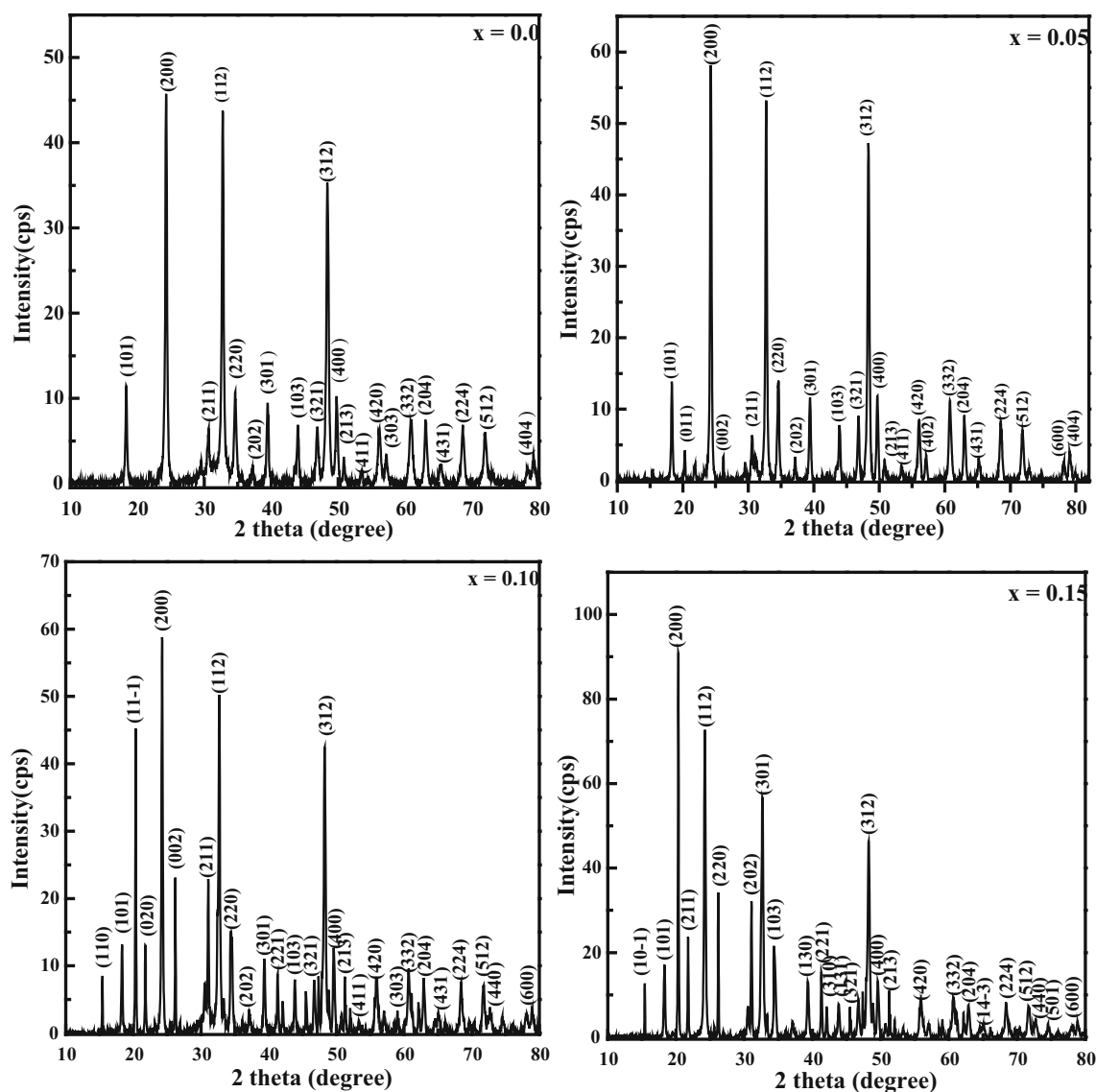


Fig. 2 Powder XRD plots for $\text{La}_x\text{Nd}_{1-x}\text{VO}_4$ ($x = 0.0, 0.05, 0.10$ and 0.15)

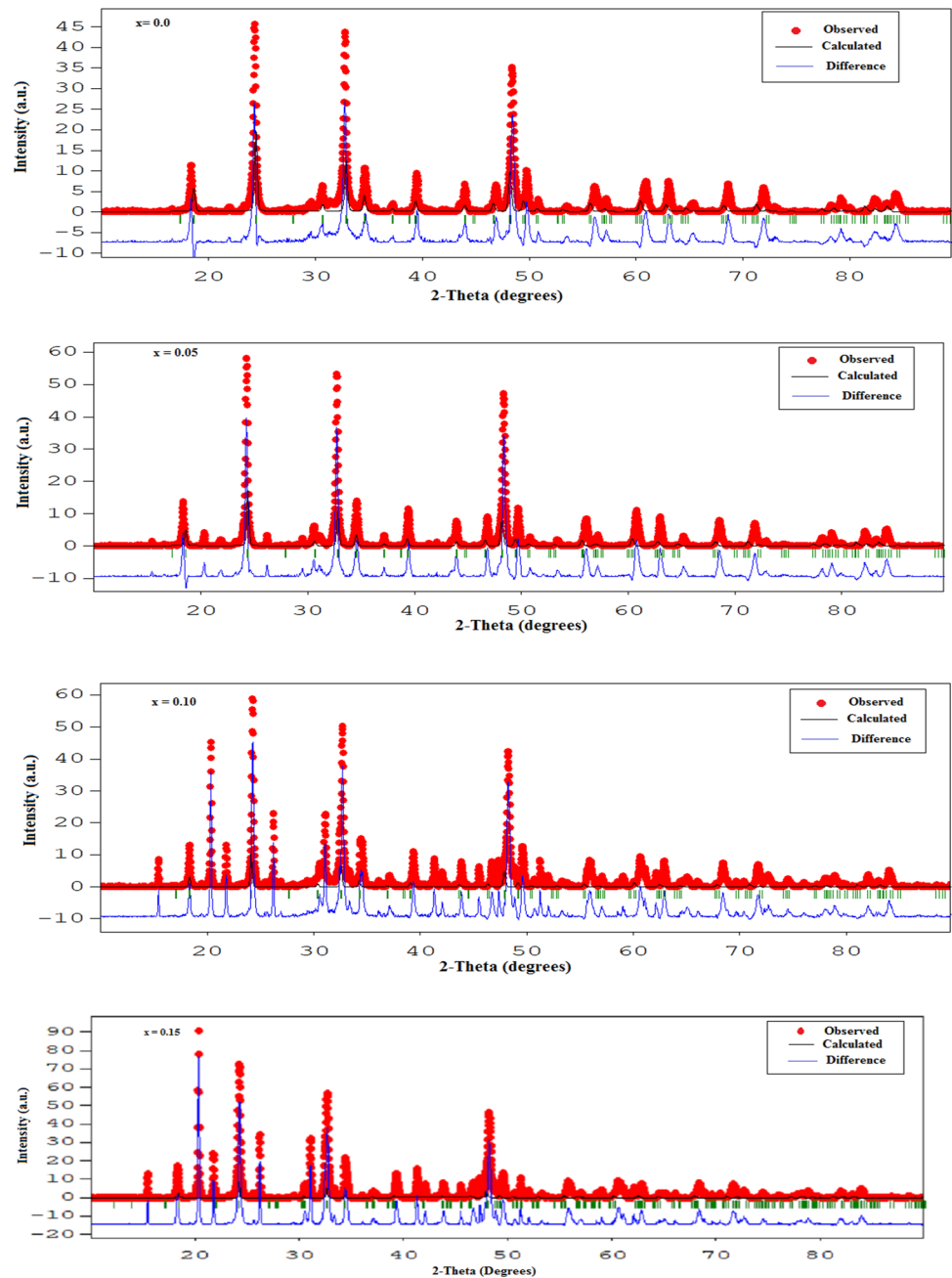
Table 1 Lattice constants, crystallite size, volume and strain (experimental and calculated) of $\text{La}_x\text{Nd}_{1-x}\text{VO}_4$

S. No.	Composition x	Lattice constant (\AA)		Crystallite size (nm)		Volume (\AA^3)	Strain (experimental)	Strain (calculated)
		$a = b$	c	Scherrer Method	Williamson–Hall Method			
1	0.0	7.32	6.42	22.86	37.45	343.9	0.0050	0.0012
2	0.05	7.32	6.43	29.11	40.76	344.5	0.0047	0.0019
3	0.10	7.33	6.36	34.35	47.79	341.7	0.0042	0.0023
4	0.15	7.34	6.32	35.01	51.30	340.4	0.0045	0.0023

performed using UV–Vis–NIR spectrophotometer: PerkinElmer Lambda 365 in the range of 200 to 800 nm, and the band gap was calculated. Room temperature photoluminescence (PL) emission spectra were recorded in the range of 400 to 800 nm using F-4700 FL spectrophotometer.

Dielectric studies were performed using impedance analyzer LCR meter SM6020, and corresponding results were obtained. To carry out the dielectric analysis, all the grown compositions were pressed into circular pellets of known diameter and thickness. Thereafter, silver paste was applied

Fig. 3 Rietveld refined PXRD patterns of La_xNd_{1-x}VO₄ ($x = 0.0, 0.05, 0.10$ and 0.15)



to both sides of the circular face of the pellets to make it conduct, followed by drying at 573 K for 1 h in a hot air oven and cooling naturally to room temperature.

3. Results and discussion

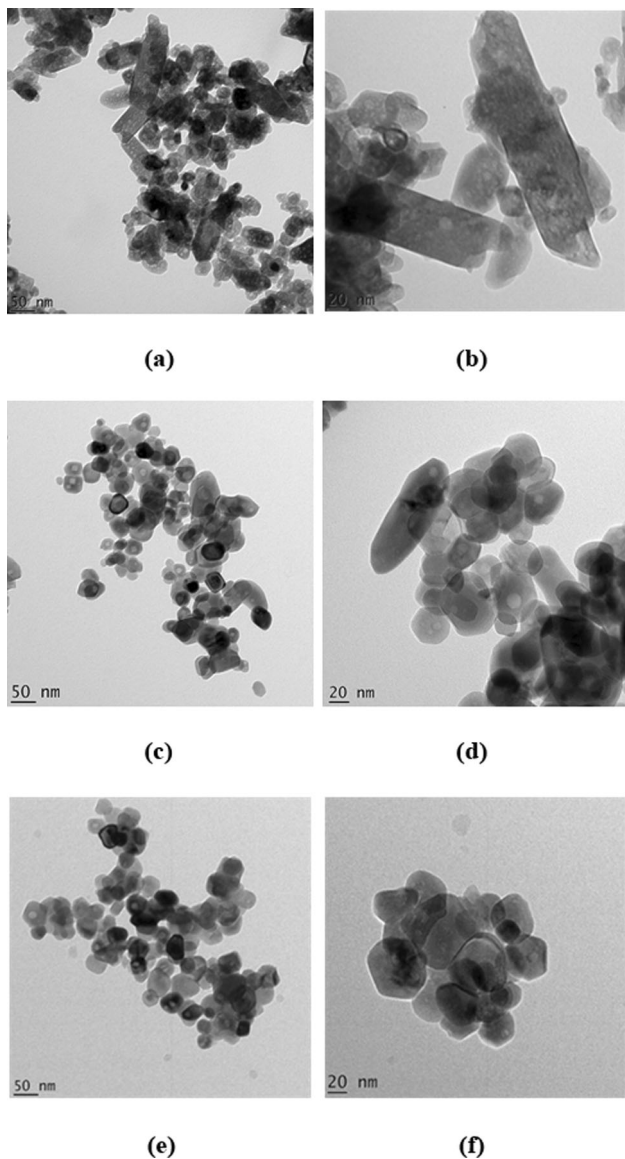
3.1. Powder X-ray diffraction (PXRD) analysis

The PXRD patterns of various compositions of prepared nanoparticles are recorded in 2θ range between 10° and 80° as shown in Fig. 2. The prepared materials are highly pure

and crystalline in nature. These high-intensity peaks are well matched with JCPDS card no. 720859 with space group I41/amd and space group no. 141. The main reflection peaks were observed for the (101), (200), (112), (220), (301) and (312) planes which are the characteristic peaks of tetragonal structure of NdVO₄. No extra diffraction peaks are seen in case of La_xNd_{1-x}VO₄ (for $x = 0.0, 0.05$). The PXRD pattern of the La_xNd_{1-x}VO₄ (for $x = 0.10$ and 0.15) shows extra diffraction peaks which are indexed to the monoclinic LaVO₄ (JCPDS card no. 500367). Similar results were obtained by Monsef et al. [16] in case of neodymium vanadate (NdVO₄) nanostructures synthesized

Table 2 Refined structural parameters obtained from Rietveld analysis

S. No.	Composition x	R_{WP} (%)	R_{EXP} (%)	R_P (%)	χ^2	Bragg R -factor (R_B)	RF-factor (R_F)
1	0.0	0.978	0.658	0.976	1.48	96.63	81.61
2	0.05	0.964	0.706	0.940	1.36	92.96	75.04
3	0.10	0.917	0.794	0.864	1.15	82.67	60.04
4	0.15	0.878	0.823	0.815	1.06	75.52	52.30

**Fig. 4** High-resolution transmission electron microscope (HRTEM) images of $\text{La}_x\text{Nd}_{1-x}\text{VO}_4$ at a resolution of 50 and 20 nm for $x = 0.0$ (a, b), $x = 0.10$ (c, d) and $x = 0.15$ (e, f) respectively

via a modified solid-state method in the presence of ligand

where two diffraction peaks indexed to the hexagonal Nd_2O_3 (JCPDS 83-1353) were seen.

The Scherrer method is the most commonly used approach to calculate the crystallite size by making use of the broadening of Bragg's lines. The crystallite size of products is calculated using the following equation [27]

$$D = K\lambda/\beta \cos \theta \quad (1)$$

where ' K ' is the shape factor and takes a value around 0.9, ' λ ' is the wavelength of X-ray radiation source and ' β ' is the full width at half maximum (FWHM) of intensity of the major peak and ' θ ' is the Bragg angle.

The Williamson–Hall method [28] is another approach to have better understanding of crystallite size and contributions of microstrains observed in the crystal lattice. The crystallite size was calculated by the Williamson–Hall method followed by strain calculations using Eq. (2)

$$\varepsilon = \beta/4 \tan \theta. \quad (2)$$

PXRD peak broadening is well related to the crystallite size and is produced due to the contributions of microstrains in the crystal lattice alone or by the combined effect of particle size and strain [29, 30]. It can be concluded from the above equation that the width of the peak varies with crystallite size as $1/\cos\theta$, whereas strain varies as $\tan\theta$. It is assumed that the contributions of crystallite size and strain to line broadening are independent of each other and the observed line width is the sum of terms as shown in equation below

$$\beta \cos \theta = K\lambda/D + 4\varepsilon \sin \theta \quad (3)$$

The above equation is known as the Williamson–Hall equation as it is attributed to G. K. Williamson and his student W. H. Hall. The graphs were plotted by taking $4\sin\theta$ along the x-axis and $\beta\cos\theta$ along the y-axis, and a straight line is obtained. The strain ' ε ' produced in the lattice was estimated from the slope of straight line, whereas crystallite size was determined from the intercept along the y-axis.

The values of unit cell parameters, volume and strain are calculated and are given in Table 1. The value of crystallite size lies in the range of 22.86 to 35.01 nm as calculated from the Scherrer method. The value of crystallite size for

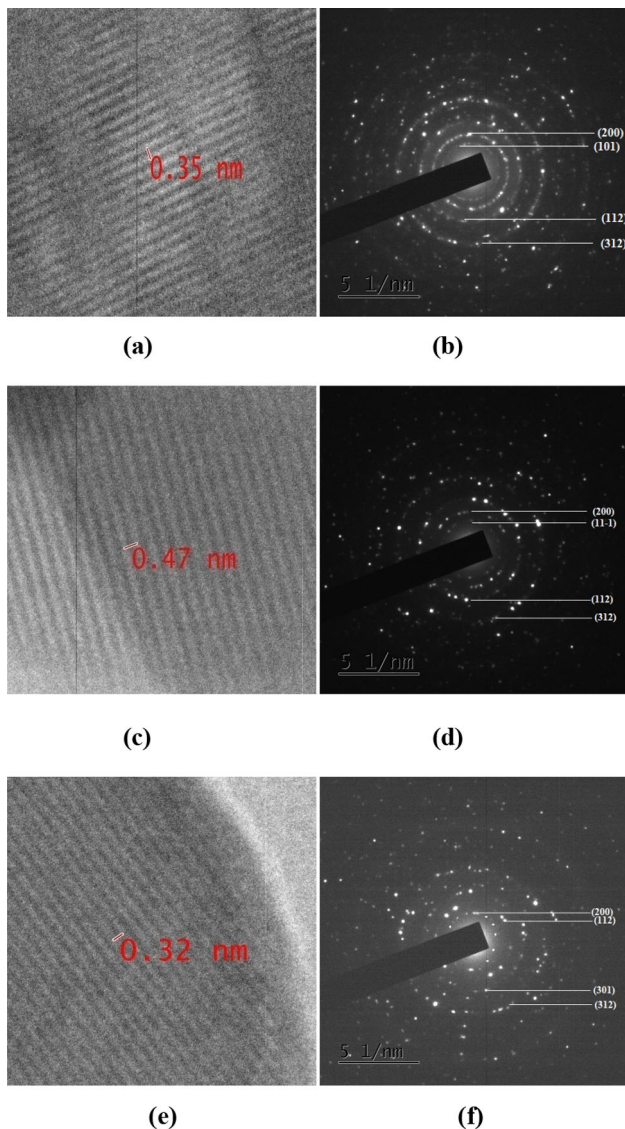


Fig. 5 High-resolution images with d-spacing values of $\text{La}_x\text{Nd}_{1-x}\text{VO}_4$ for (a) $x = 0.0$, (c) $x = 0.10$ and (e) $x = 0.15$, respectively. Selected area electron diffraction (SAED) pattern with indexing of various planes of $\text{La}_x\text{Nd}_{1-x}\text{VO}_4$ for (b) $x = 0.0$, (d) $x = 0.10$ and (f) $x = 0.15$, respectively

NdVO_4 has been reported to be 14 nm [9]. Thus, on comparing these two results, the value of crystallite size is found to slightly increase in the present case. From the table, it is clear that the crystallite size increases with doping concentration because the atomic radius of dopant (here dopant is La) is greater than that of host (here host is Nd).

The PXRD patterns were further analyzed by employing the Rietveld refinement method with the help of full-proof software, and the refined PXRD patterns are shown in Fig. 3. Reliability factors, viz. weighted profile factor (R_{WP}), R expected (R_{Exp}), profile factor (R_{P}), goodness factors (χ^2), Bragg R-factor (R_{B}) and RF-factor (R_{F}) related

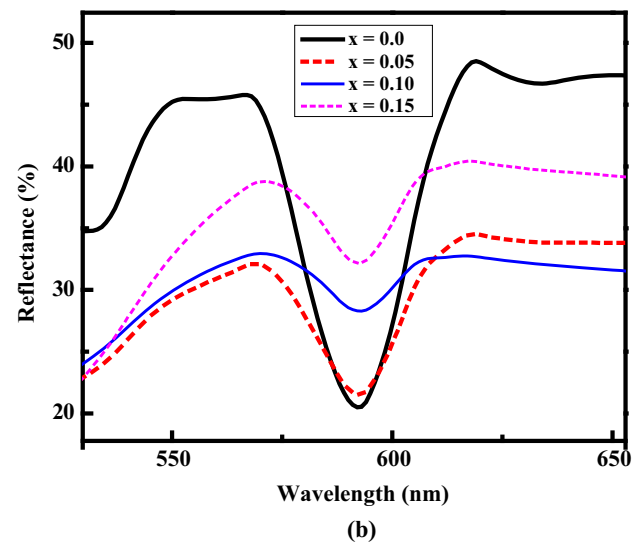
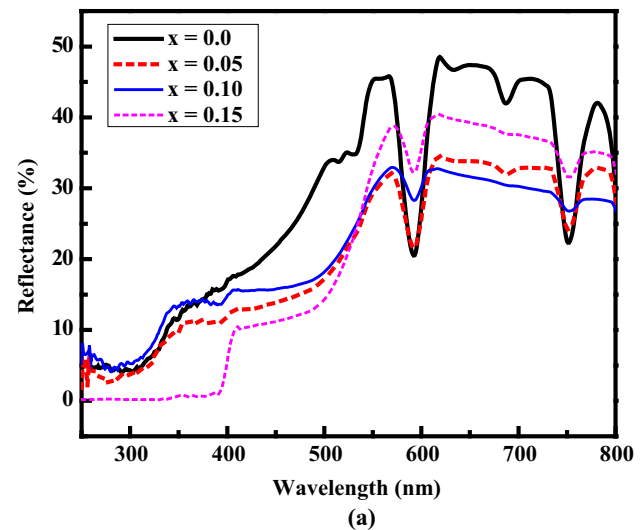


Fig. 6 (a) Diffused reflectance spectra of $\text{La}_x\text{Nd}_{1-x}\text{VO}_4$ ($x = 0.0, 0.05, 0.10$ and 0.15). (b) Enhanced view of spectra in the range 500 nm to 600 nm

to quantitative analysis of PXRD patterns by Rietveld refinement, were calculated and are shown in Table 2. The ratio of R_{WP} and R_{Exp} gives the value of χ^2 by using Eq. (4) [31]:

$$\chi^2 = (R_{\text{WP}}/R_{\text{Exp}}) \quad (4)$$

The better quality of refinement will be considered reliable only when $1 \leq \chi^2 < 2$. The quantity R_{WP} mainly depends on the background of the pattern instead of intensity values. The low values of χ^2 and profile parameters (R_{P} , R_{WP}) suggest that the prepared samples are of better quality and refinements of samples are effective and reliable [32].

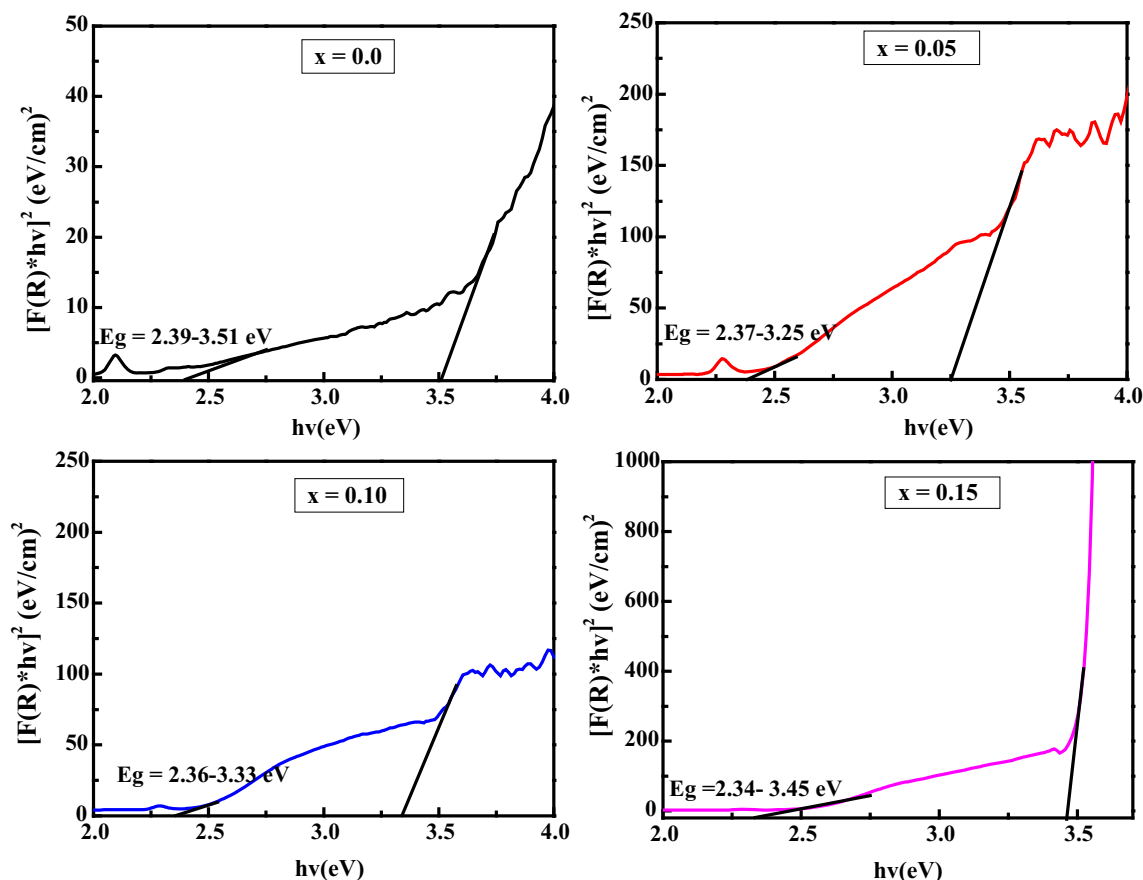


Fig. 7 Optical energy band gap of $\text{La}_x\text{Nd}_{1-x}\text{VO}_4$ ($x = 0.0, 0.10, 0.10$ and 0.15)

3.2. TEM and SAED analysis

To study size and morphology of prepared compositions, high-resolution transmission electron microscopy (HRTEM) supplemented with selected area electron diffraction (SAED) analysis has been employed. Figure 4(a & b) shows the morphology of NdVO_4 composition, i.e., $x = 0.0$ at two different resolutions. These images show the appearance of varying morphologies with partial agglomeration where rod shaped morphology predominates. Tian et al. [15] observed the formation of nanorod arrays with ultrasonic treatment showing the self-assembly of NdVO_4 nanorods. In our studies, nanoarrays as such are not observed rather few nanorods are seen with the presence of varying morphology. Figure 4(c & d) shows the formation of distinct nanoparticles having a dominated elongated spherical structure along with rod shape morphology for $x = 0.10$. As La^{3+} is doped into the reaction system, it is found that dominance of nanorod-shaped features no longer holds. With increasing doping concentration of La to 15% ($x = 0.15$), no more rod-shaped features were observed. As seen from the micrograph, hexagonal-shaped porous features are observed on the surface of nanoparticles as shown

in Fig. 4 (e & f). Similar types of results were reported for CeVO_4 [33]. Comparative analysis of grown compositions shows that the morphology changes with varying concentration of La^{3+} ions from rod-shaped to hexagonal-shaped porous features. The average grain size of three compositions of $\text{La}_x\text{Nd}_{1-x}\text{VO}_4$ varies between 20 and 40 nm which confirms that the prepared materials are of nanometer size as desirable. On comparing size obtained by PXRD and HRTEM, it is found that PXRD size is usually equals or smaller than TEM size [34]. From PXRD one can determine crystallite size and HRTEM gives a specified grain size. The association of several crystallites leads to the formation of grains. Thus, difference between calculated particle sizes by powder XRD and HRTEM analysis is very much related to the correlation between crystallite and grain [35, 36].

Figure 5(a,c and e) shows the higher-resolution images for all the compositions indicating the clear d-spacing of 0.35, 0.42 and 0.32 nm corresponding to (200), (101) and (220) planes of tetragonal phase of $\text{La}_x\text{Nd}_{1-x}\text{VO}_4$ nanoparticles where $x = 0.0, 0.10$ and 0.15 , respectively. The excellent matching of the d-spacing values with those of literature confirms the tetragonal phase of neodymium

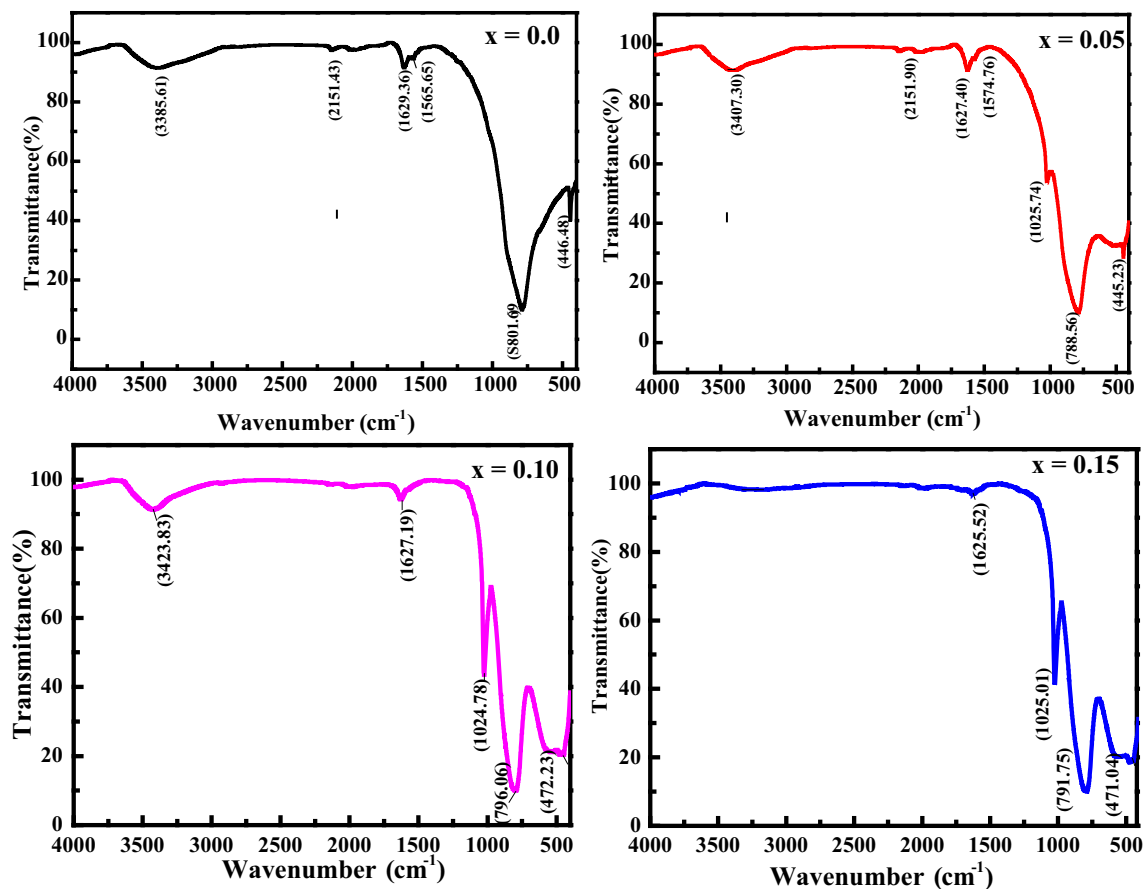


Fig. 8 Fourier transform infrared (FTIR) spectrum depicting various functional group present in La_xNd_{1-x}VO₄ ($x = 0.0, 0.05, 0.10$ and $x = 0.15$)

vanadates nanoparticles and these are in good agreement with the PXRD results.

Figure 5(b, d and f) shows the selected area electron diffraction (SAED) pattern of the three compositions La_xNd_{1-x}VO₄ (where $x = 0.0, 0.10$ and 0.15 , respectively) which confirms the crystallinity and orientation of the prepared materials. From the SAED pattern, the diffraction rings are indexed to various planes corresponding to sharp and high-intensity peaks of PXRD pattern. The indexing of these rings further confirms the tetragonal phase of the prepared compositions. The diffractions rings are in good agreement with the powder XRD results and confirm the tetragonal structure of these materials by indexing of diffraction spots.

The crystallinity index equation was used to evaluate crystallinity index [37]

$$I_{\text{crys}} = D_{\text{g}}/D_{\text{crys}} \quad (5)$$

where I_{crys} is the crystallinity index, D_{g} is the grain size obtained from HRTEM analysis and D_{crys} is the crystallite size obtained by the Scherrer method. Here, value of I_{crys} is calculated and comes out to be 1.15, 1.01 and 1.14 for La_xNd_{1-x}VO₄ (where $x = 0.0, 0.10$ and 0.15 , respectively),

which is slightly greater than 1 in all the compositions. Hence, these materials are polycrystalline in nature.

3.3. UV-Vis analysis

Figure 6(a) shows the UV-Vis diffused reflectance spectrum in case of La_xNd_{1-x}VO₄. The diffused reflectance is observed to decrease with an increase in doping concentration in the visible range between 500 to 600 nm as shown in Fig. 6(b) [38]. The Kubelka-Munk absorption coefficient (K/S) was calculated from the observed reflectance spectra by using Eq. (6)

$$(\alpha h\nu)^{1/2} = K/S = (1 - R)^2/2R \quad (6)$$

where ' K ', ' S ' and ' R ' represent the absorption coefficient, scattering coefficient and reflectivity, respectively. This high absorption in the desired visible range finds many potential applications for the hetero-structure, such as in the fabrication of optoelectronic devices and solar cells. From the plot of reflectance versus energy, the band gap for all compositions was calculated. The optical band gap values obtained from the diffuse reflectance spectra are found to be in the range of 2.39–3.51, 2.37–3.25, 2.36–3.33

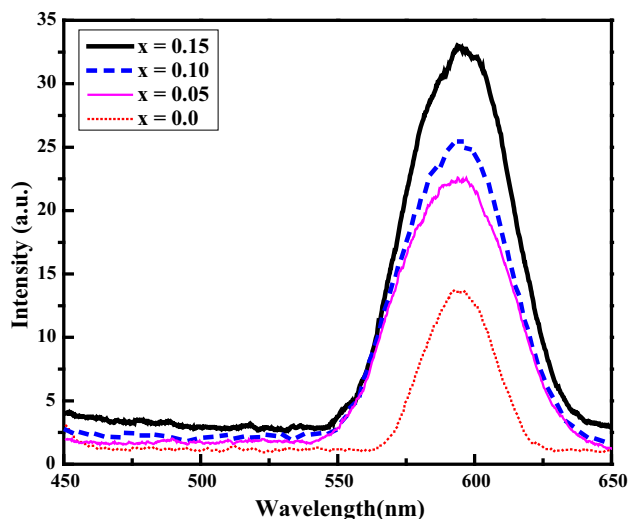


Fig. 9 Photoluminescence (PL) emission spectrum of $\text{La}_x\text{Nd}_{1-x}\text{VO}_4$ ($x = 0.0, 0.05, 0.10$ and 0.15) using excitation wavelength ($\lambda_{\text{exc}} = 350$ nm)

and 2.34–3.45 eV for $\text{La}_x\text{Nd}_{1-x}\text{VO}_4$ where $x = 0, 0.05, 0.10$ and 0.15 , respectively, as shown in Fig. 7. The band gap of the neodymium vanadate nanopowders was calculated to be 3.50 eV by Dragomir and Valant [13]. These results confirm that NdVO_4 is a wide-gap semiconductor (2–4 eV) and its attractive properties make it a promising candidate for electronic applications. The calculated values of band gap are comparable to the band gap value of the well-known photocatalyst, TiO_2 . Hence, the orthovanadates could act as photocatalysts under UV light [13]. Also comparing the results of two studies leads to the conclusion that the optical band gap is slightly reduced in present study. The optical band gap increases or decreases according to the density of localized states: low or high, respectively. PXRD and HRTEM are useful techniques to produce the details of localized states. In the present research work, the intensity of PXRD increases and the full width at half maxima (FWHM) decreases with the increasing doping ratio. This gives more enhancements of order and the localized states or defects decreases with an increase in dopant concentration which means an increase in crystallite size. The crystallite size increases with an increase in doping concentration as explained in the powder XRD results. So, this explains the usual phenomenon behind the decrease of energy band gap with an increase in doping concentration. Thus, powder XRD results are in good agreement with the UV–Vis spectroscopy results.

3.4. Fourier transform infrared (FTIR) analysis

The functional groups of synthesized NdVO_4 nanoparticles analyzed by FTIR spectra recorded in the region of 400–4000 cm^{-1} are shown in Fig. 8. The FTIR

spectroscopy of all compositions was conducted to explore chemical interactions and bonding structures. VO_4 stretching vibration can be observed at 446.48, 445.23, 472.23 and 471.04 cm^{-1} for compositions $\text{La}_x\text{Nd}_{1-x}\text{VO}_4$ where $x = 0.0, 0.05, 0.10$ and 0.15 respectively. V–O bond has appeared at 801.69, 788.56, 796.06 and 791.75 cm^{-1} , respectively, for the four compositions [39]. Another band around 1629.36 to 1565.65, 1627.40 to 1574.76, 1627.19 and 1625.52 cm^{-1} , respectively, corresponds to the bending vibration of the hydrogen bonded OH groups of water in all the compositions as shown in the figure [40]. The broad band around 3358.48, 3407.30 and 3423.82 cm^{-1} can be assigned to the stretching vibrations of surface water in case of $\text{La}_x\text{Nd}_{1-x}\text{VO}_4$ (where $x = 0, 0.05, 0.10$). No such band is observed in case of 15% composition. As the intensity of absorption band depends on the change in the dipole moment of the bond associated with the vibration and greater the change in dipole moment, the more intense is the absorption. This signifies that the change in dipole moment associated with hydroxyl units is negligible in case of $x = 0.15$.

Monsef et al. [16] carried out FTIR analysis of neodymium vanadate nanoparticles and obtained V–O bond, bending vibrations of OH groups of water and stretching vibrations of OH groups attached to the surface of nanoparticles at around 807, 1634 and 3447 cm^{-1} respectively. Thus, comparing the results obtained in the present case with those obtained by Monsef et al., it can be seen that various peaks and bands have shifted to the low wavenumber region. This is because of an increase in bond length. Bond length changes may occur due to the change in electronegativity of the neighboring atom and can be attributed to the lattice contraction of the vanadate structure in the present study, which leads to an increase in the bond length [41]. Thus, the shift in various peaks and bands confirms there is an interaction between the host and dopant and these observed functional groups further support the successful formation of $\text{La}_x\text{Nd}_{1-x}\text{VO}_4$ nanoparticles.

3.5. Photoluminescence studies

Figure 9 shows the photoluminescence (PL) spectra at room temperature between 450 and 650 nm with an excitation wavelength of 350 nm. PL spectra of NdVO_4 have been reported in the literature [42]. Most of the reported spectra show sharp peaks in the range of 400–700 nm with different intensities and peak positions. In case of tetragonal zircon NdV nanomaterials, the Nd^{3+} ions are placed at sites that do not possess center of symmetry (D_{2d} symmetry) [43]. This leads to electronic dipole transitions within the $\text{Nd}^{3+} 4f$ shells resulting in emission bands in the visible region centered at around 594 nm [15] as shown in

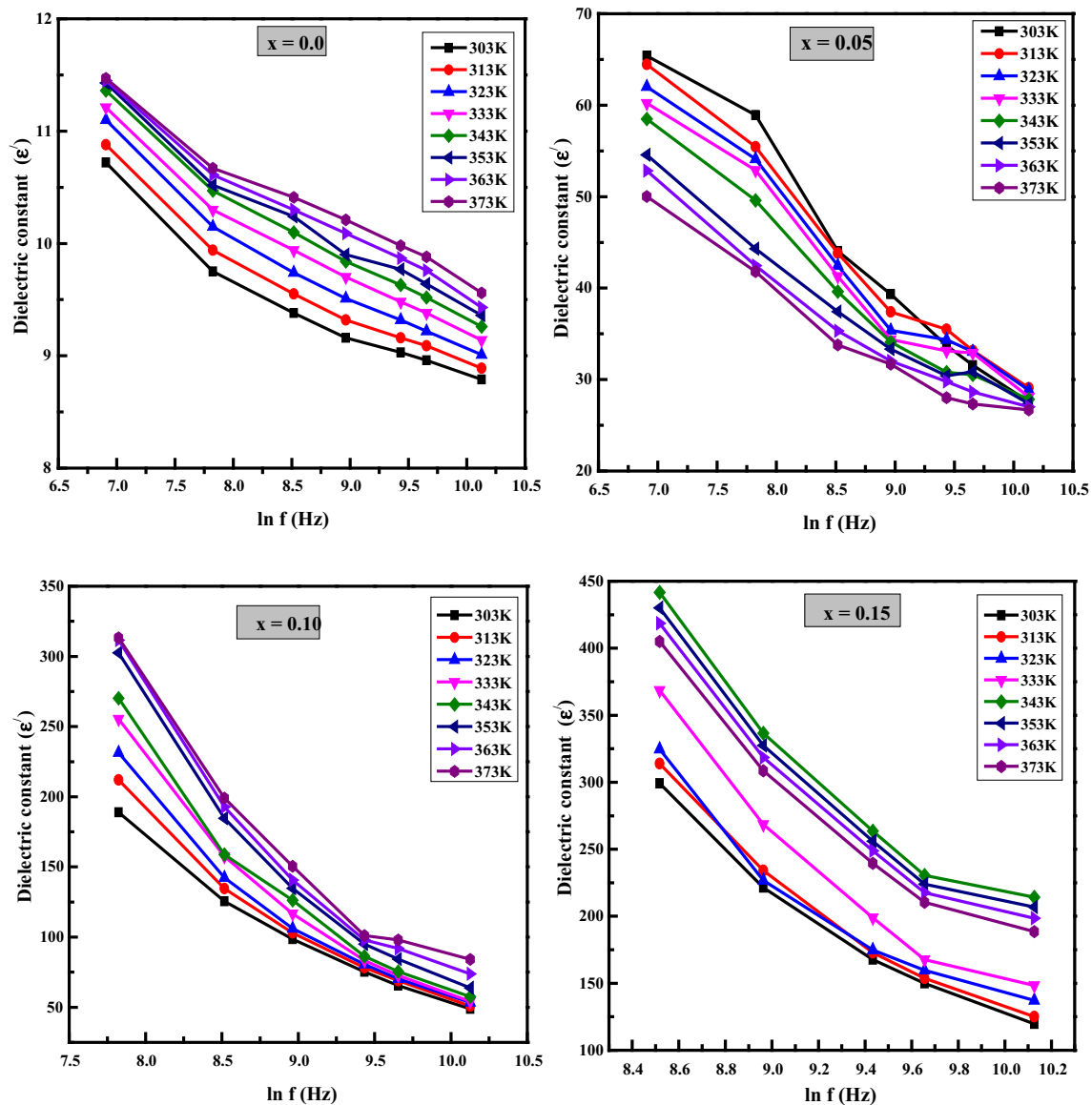


Fig. 10 Graph showing the variation of dielectric constant with frequency (f) at different temperatures for $\text{La}_x\text{Nd}_{1-x}\text{VO}_4$ ($x = 0.0, 0.05, 0.10$ and 0.15)

the figure. A sharp and highly intense peak observed around 594 nm is attributed to $({}^2G_{9/2} - {}^4G_{11/2}) \rightarrow {}^4I_{13/2, 15/2}$ and $({}^4G_{7/2} - {}^4G_{9/2}) \rightarrow {}^4I_{11/2, 13/2}$ transitions. From the results, it can be analyzed that the trend of PL intensity with La^{3+} doping is the same. As the doping concentration of La^{3+} is increased, the integrated intensity gradually increases. This implies that more La^{3+} ions are incorporated into the host lattice at a higher doping concentration of La^{3+} (15%) leading to prominent energy migration between the La^{3+} ions [44]. Similar trend in these results have been reported in the literature [10]. The integrated intensity is found to increase gradually with the Eu^{3+} doping. Likewise, the increasing concentration of La^{3+} ions leads to an increase in intensity of PL spectra. On comparison of PL intensity

and crystallite size of four compositions, it is observed that PL intensity increases with increasing crystallite size. High dopant concentrations produce large crystallite sizes as confirmed by the Scherrer's equation from the PXRD pattern. The increase in PL intensity with increasing crystallite size is in agreement with the results reported by Purwanto et al. [45].

3.6. Dielectric studies

The real part (ϵ') of dielectric constant is obtained from the measured values of parallel capacitance (C_p) by the relation [46]

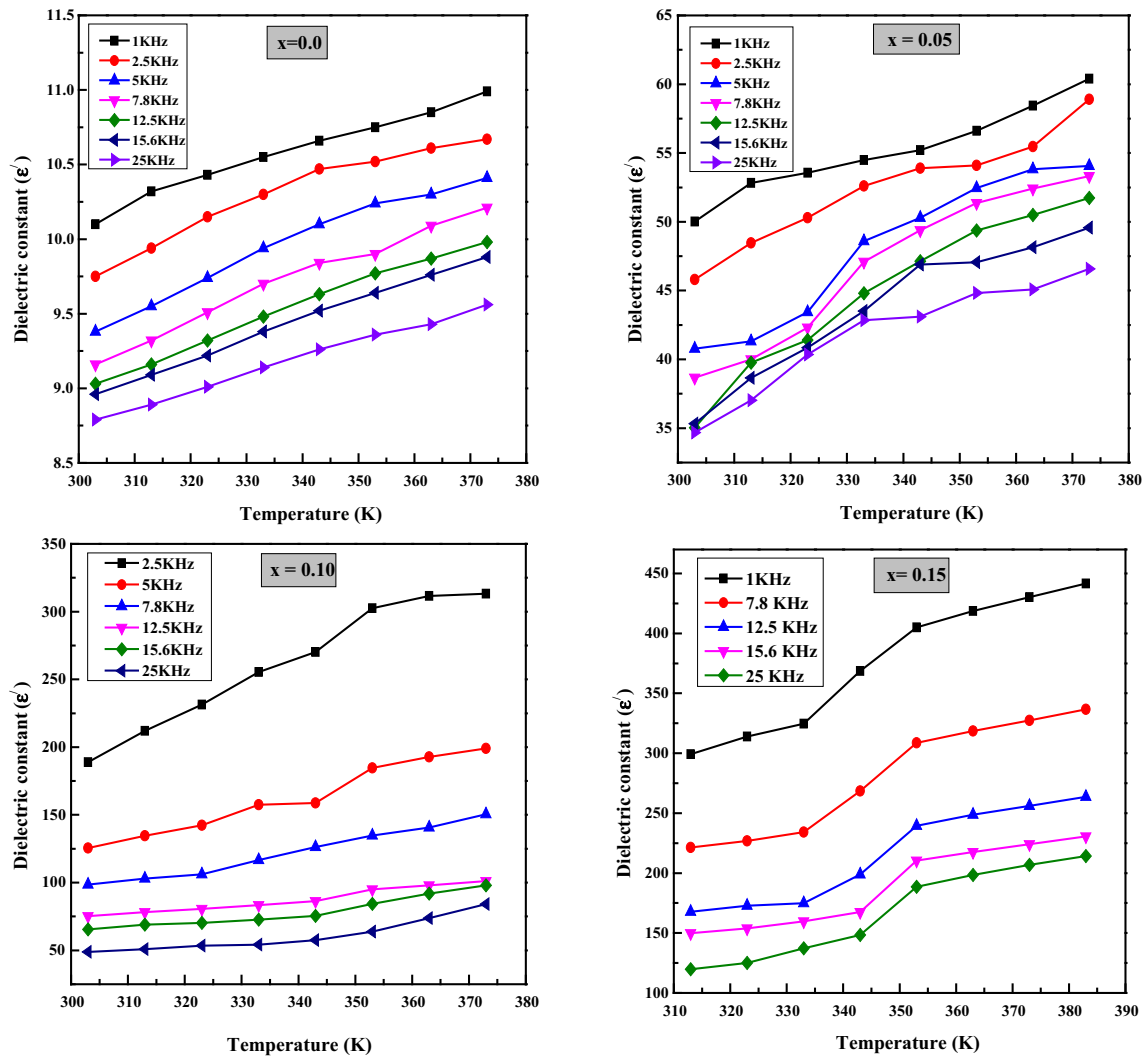


Fig. 11 Graph showing the variation of dielectric constant with temperature at different frequencies for $\text{La}_x\text{Nd}_{1-x}\text{VO}_4$ ($x = 0.0, 0.05, 0.10$ and 0.15)

$$\epsilon' = C_p t / A \epsilon_0 \quad (7)$$

Here ' t ' is the thickness, ' A ' represents the cross-sectional area of the sample, ' ϵ_0 ' denotes the permittivity of free space having a value of $8.854 \times 10^{-12} \text{Fm}^{-1}$, and ' D ' is dielectric loss and can be written as $\tan \delta$ (dielectric loss tangent).

Figure 10 shows the dielectric constant (ϵ') versus frequency curve at different temperatures. The values were taken at a temperature interval of 10 K and a maximum temperature of 373 K for all four compositions. From plots of all compositions, it is observed that the ϵ' decreases with an increase in frequency, i.e., the dielectric constant is high at low frequencies and decreases with the applied frequency at all temperatures. The dielectric constant values drops with the rise in frequency and reach the almost low limiting value. The observed phenomenon can be ascribed to the oscillations of free dipoles in an alternating electric

field. The ϵ' is inherently the outcome of the electronic, ionic and space charge polarization [46]. At lower frequencies, dispersion of ϵ' arises due to the space charge polarization and orientation polarization of dipoles. As the frequency increases, the dipoles no longer satisfactorily rotate and their oscillations commence to lag those of the electric field. With further increase in frequency, the dipoles could not follow the field completely and the orientation polarization ceases and the value of ϵ' reduces to a low value at higher frequencies [47]. In general, it is seen that as frequency increases, the dielectric constant of the material decreases, because its net polarization drops as each polarization mechanism ceases to contribute.

Figure 11 shows the dielectric constant (ϵ') versus temperature curve at different frequencies. The dielectric constant is found to increase with temperature at all frequencies for all compositions. The phenomenon of the

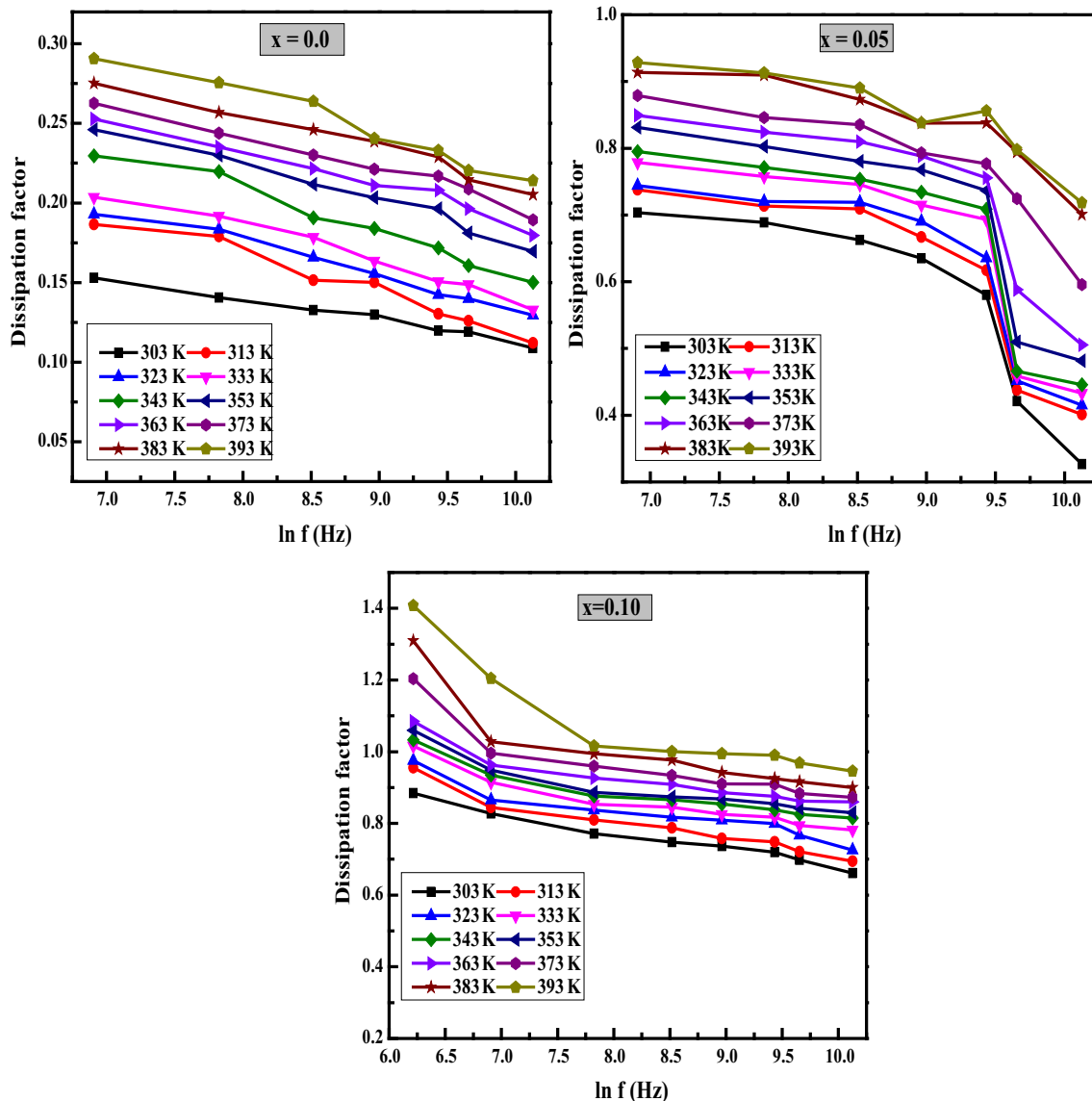


Fig. 12 Graph showing the variation of dissipation factor with frequency (f) at different temperatures for $\text{La}_x\text{Nd}_{1-x}\text{VO}_4$ ($x = 0.0, 0.05$ and 0.10)

increasing nature of ϵ' with a rise in temperature is generally related to the reduction in bond energies [48]. This could be explained in terms of relationship between effects on dipolar polarization and a rise in temperature. The orientation of dipole is usually eased with temperature rise, and this results in an increase in the dielectric constant with temperature [47]. From the graphs, it is clearly seen that the dielectric constant increases with an increase in dopant concentration (i.e., increasing La^{3+} concentration from 5 to 15%).

Figure 12 shows the variation of dissipation factor (dielectric loss) with respect to frequency at different temperature values. It is observed that dissipation factor decreases with rise in frequency for the composition $\text{La}_x\text{Nd}_{1-x}\text{VO}_4$ (where $x = 0, 0.05, 0.10$) whereas dielectric

loss (dissipation factor) was not observed in case of $x = 0.15$. The large value of dissipation factor at low frequency is due to dipole polarization. Thereafter, migrations of small polarons or ions occur leading to a drop in dielectric loss at higher frequencies. Also with increasing frequency, the accumulation of charges at the interface is not seen due to which the value of dissipation factor reduces to its lowest value. It is analyzed from these plots that the dielectric loss initially showed a decreasing trend with a rise in frequency and became more or less constant at higher frequencies values (i.e., 25 kHz) except in case of $x = 0.05$ where the decrease was prominent at higher frequencies. Such a trend of variations demonstrates that losses are the characteristics of dipole mechanism [49].

In the present study, it is observed that the value of dielectric constant ranges between 8 and 12 in case of $x = 0.0$ composition. Verma et al. [43] studied this type of response in neodymium vanadate nanoparticles. The value of the dielectric constant for other compositions in the present case varies between 25 and 70, 50 and 325 and 100 and 450 for $x = 0.05, 0.10$ and 0.15 , respectively. Thus, the dielectric constant increases with an increasing La^{3+} (dopant) concentration. Similar results have been reported in case of LaVO_4 with an increase in Sr concentration [50]. Comparative analysis of two studies shows that there is an increase in dielectric constant, particularly at higher doping. The significance of high value of dielectric constant leads to power application of these materials as they may empower gadget scaling down (device miniaturization).

4. Conclusions

The neodymium vanadate and lanthanum-doped neodymium vanadate nanoparticles were effectively synthesized using a solution based facile room temperature co-precipitation method. This method is simple to use and conserves energy since it does not require any complex thermal treatment. This approach could potentially be employed for the facile preparation of other lanthanide vanadate structures. The synthesis process makes use of aqueous solutions of $\text{La}(\text{NO}_3)_3$, $\text{Nd}(\text{NO}_3)_3$ and NH_4VO_3 as a precipitating agent. The powder XRD method confirmed the synthesis of impurity free, crystalline nanoparticles with tetragonal structure, space group I41/amd and space group no. 141. The average crystallite size obtained from the Scherrer formula and the Williamson–Hall method increases with an increase in the doping concentration of lanthanum. Rietveld analysis was carried out on PXRD data using full-proof software. The lower values of profile parameters such as R_p , R_{wp} and χ^2 confirmed that the calculated diffraction pattern is in good agreement with the observed pattern. The size and morphology of synthesized nanoparticles were explained with the help of HRTEM analysis and the SAED pattern confirmed the crystallinity and orientation of the prepared materials. HRTEM results were found to be in good agreement with the PXRD results. The presence of various functional groups was confirmed with the help of FTIR spectroscopy. UV–Vis analysis of prepared materials was carried out to study the diffuse reflectance spectrum, and the optical energy band gap values were calculated. UV–Vis spectroscopy and PXRD results were found in good agreement with each other. Photoluminescence (PL) studies show that the integrated intensity gradually increases as the doping concentration of La^{3+} is increased. Dielectric studies show that the dielectric constant decreases with an increase in frequency and it

decreases with temperature at different frequencies for all four compositions. The dissipation factor, i.e., dielectric loss, is calculated and is found to decrease with increasing frequency at various temperatures. Further, it is observed that increasing dopant concentration increases the dielectric constant of the materials. Therefore, in conclusion one can say that the main novelty of this work is the preparation of a simple and cost-effective solution based technique to prepare neodymium vanadate and lanthanum-doped neodymium vanadate nanoparticles without the use of surfactant so that various properties of these materials can be studied in depth and can be employed for various potential applications. Among the potential applications identified is the use of rare earth vanadates, $\text{La}_x\text{Nd}_{1-x}\text{VO}_4$ to act as the suitable photocatalysts under UV light. Apart from this, such materials can be employed for high performance optoelectronic devices and dopants in glass and optical fibers. Due to their enhanced value of dielectric constant, lanthanum-substituted ceramic material can be employed for its possible applications at microwave frequencies.

Acknowledgements The authors express their sincere thanks and gratitude to the Sophisticated Test and Instrumentation Centre (STIC), Cochin University, for providing the facilities of powder X-ray diffraction (PXR), high-resolution transmission electron microscopy supplemented with selected area electron diffraction (HRTEM–SAED) and Fourier transform infrared (FTIR) spectrophotometer. The corresponding author also acknowledges the Research & Seed Grant given to the CGMR laboratory by University of Jammu under the Head Quality Assurance Fund (DIQA), RUSA 2.0 and PURSE grants.

Author contributions All the authors contributed toward studying this problem. Material preparation, data collection and analyses were performed by Monika and Bindu Raina. Mitesh Solanki and Bharat Parekh contributed to the X-ray diffraction and Rietveld analysis. The first draft of the manuscript was written by Monika. Prof. K.K. Bamzai supervised and conceived the problem. All the authors read and approved this manuscript.

Data availability The data sets generated and analyzed during the current study are available from the corresponding author on reasonable request.

Declarations

Conflict of interest The authors declare no conflict of interest.

References

- [1] V Zepf Chapter 1 *Rare earths Industry* (Boston: Elsevier) (2016). <https://doi.org/10.1016/B978-0-12-802328-0.00001-2>
- [2] G Wang, Q Peng and Y Li *Acc. Chem. Res.* **44** 322 (2011)
- [3] B C Chakoumakos, M M Abraham and L A Batner *J Solid State Chem.* **109** 197 (1994)
- [4] M Prasad, A Pandit, T H Ansari, R A Singh and B M Wanklyn *Phys Lett.* **138** 61 (1989)

- [5] B H T Chai, G Loutts, X X Chang, P Hong, M Bass, I A Shcherbakov and A I Zagumennyi: *Advanced solid state lasers*, Technical digest Washington (DC): *Optical Society of America*. **20** 41 (1994)
- [6] K Byrappa, K Rai, B Nirmala and M Yoshimura *Mater Sci Forum*. **506** 315 (1999)
- [7] A Nag, D Ghosh and B M Wanklyn *Solid State Commun*. **108** 265 (1998)
- [8] S Balasubramanian, J N Baby and Y F Hsu *Chem. Eng. J.* **451** 138694 (2023)
- [9] M Vosoughifar *J. Mater. Sci. Mater. Electron*. **27** 7384 (2016)
- [10] V Panchal, D Errandonea, F J Manjon, A Munoz, H P Rodriguez, S N Achary and A K Tyagi *J. Phys. Chem. Sol.* **100** 126 (2017)
- [11] L Wei, F Liang, S Yi-hu and T Ying *J. Electr. Mat.* **4** 46 (2017)
- [12] S Balasubramanian, J N Baby and Y F Hsu *J. Electrochem. Soc.* **169** 087508 (2022)
- [13] M Dragomir and M Valant *Acta Chim. Slov.* **65** 679 (2018)
- [14] M M Saad and A Ehlag *Indian J. Phys.* **96** 2731 (2022)
- [15] L Tian, S Chen and Q Liu *Trans. Nonferrous Met. Soc. China* **30** 1031 (2020)
- [16] R Monsef, M G Arani and M S Niasari *J Environ. Manag.* **230** 266 (2019)
- [17] N O Nunez, P Zambrano and J G Sevillano *Eur. J. Inorg. Chem.* **27** 4546 (2015)
- [18] P Kumari, P K Baitha and J Manam *Indian J. Phys.* **89** 1297 (2015)
- [19] D R Kamble, S V Bangale and S R Bamane *Nanosyst. Phys. Chem. Math.* **12** 199 (2021)
- [20] M Ying, J Hou, W Xie, Y Xu, S Shena, H Pan and M Du *Sens. Actuators B* **260** 125 (2018)
- [21] S Thakur and A K Gathania *Indian J. Phys.* **89** 973 (2015)
- [22] Saloni and A Khanna *J. Mater. Sci.: Mater. Electron* **34** 70 (2023)
- [23] S Ghotekar, S Pansambal, K Y Andrew, D Pore and R Oza *Top. Catal.* **66** 89 (2023)
- [24] H Aijiang, L Feng, L Liu, J Peng, Y Chen, L Xuhao, L Wencong and L Junyang *J. Mater. Sci. Mater. Electron*. **31** 13131 (2020)
- [25] S B Narang, D Kaur and S Bahel *Mater. Lett.* **60** 3179 (2006)
- [26] <https://www.azonano.com/article.aspx?ArticleID=3285>
- [27] B D Cullity *Elements of X-Ray Diffraction*, second ed., (Philippines: Addison- Wesley Publishing Company) (1978)
- [28] W H Hall and G K Williamson *Proc. Phys. Soc. B* **64** 937 (1951)
- [29] P C Dey and R Das *Indian J. Phys.* **92** 1099 (2018)
- [30] A R Stokes and A J Wilson *Proc. Phys. Soc.* **56** 174 (1944)
- [31] A A Bagade, V V Ganbavle, S V Mohite, T D Dongale, B B Sinha and K Y Rajpure *J. Colloid Interface Sci.* **497** 181 (2017)
- [32] S Anand, S Pauline, V M Vinosel and M A Janifer *Mater. Today Proc.* **8** 476 (2019)
- [33] D R Kamble, S V Bangale, S K Ghotekar and S R Bamane *J. Nanostruct.* **8** 144 (2018)
- [34] S Mahapatra, G Madras and T N Guru *Ind. Eng. Chem. Res.* **46** 1013 (2007)
- [35] B Akbari, M P Tavandashti and M Zandrahimi *Iran J. Mater. Sci. Eng.* **8** 48 (2011)
- [36] T Ungar, G Tichy, J Gubicza and R J Hellmig *Powder Diffr.* **20** 366 (2005)
- [37] X Pan, I M Ramirez, R Mernaugh and J Liu *Colloids Surf.* **B77** 82 (2010)
- [38] R K Selvan, A Gedanken, P Anilkumar, G Manikandan and C Karunakaran *J. Clust. Sci.* **20** 291 (2009)
- [39] C T Au, W D Zhang and H L Wan *Catal. Lett.* **37** 241 (1996)
- [40] R S Dubey and S Singh *Res. Phys.* **71** 283 (2017)
- [41] N Deligne, V Gonze, D Bayot and M Devillers *Eur. J. Inorg. Chem.* **6** 896 (2008)
- [42] V Panchal, D Errandonea, A Segura, P R Hernandez, A Muñoz, S L Moreno and M Bettinelli *J. Appl. Phys.* **110** 043723 (2011)
- [43] S Verma, R Gupta and K K Bamzai *Mater. Res. Bull.* **81** 71 (2016)
- [44] S Suresh and C Arunsheshan *Appl. Nanosci.* **4** 179 (2014)
- [45] A Purwanto, W N Wang, I W Lenggoro and K Okuyama *J. Electrochem. Soc.* **91** 154 (2007)
- [46] H M El Mallah *Acta Physica Polonica A* **122** 174 (2012)
- [47] A S Das and D Biswas *Mater. Res. Express* **6** 075206 (2019)
- [48] M Nascimento and S Watanabe *J. Phys.* **36** 795 (2006)
- [49] A Mansingh, R P Tandon and J K Vaid *Phys. Rev. B* **21** 4829 (1980)
- [50] K Sultan, R Samad and F Nazar *Adv. Mater. Lett.* **12** 21061640 (2021)

Publisher's Note Springer Nature remains neutral with regard to jurisdictional claims in published maps and institutional affiliations.

Springer Nature or its licensor (e.g. a society or other partner) holds exclusive rights to this article under a publishing agreement with the author(s) or other rightsholder(s); author self-archiving of the accepted manuscript version of this article is solely governed by the terms of such publishing agreement and applicable law.